Applied Surface Science 534 (2020) 147571

Contents lists available at ScienceDirect

Applied Surface Science

journal homepage: www.elsevier.com/locate/apsusc

Dependence of photocatalysis on electron trapping in Ag-doped flowerlike rutile-phase TiO_2 film by facile hydrothermal method

N.K.A. Hamed[a], M.K. Ahmad[a,*], N.H.H. Hairom[b], A.B. Faridah[c], M.H. Mamat[d], A. Mohamed[e], A.B. Suriani[e], N. Nafarizal[a], F.I.M Fazli[a], S.M. Mokhtar[a,f], W.I.W. Omar[a,f], M. Shimomura[f]

[a] Microelectronics and Nanotechnology-Shamsuddin Research Center, Institute for Integrated Engineering, Universiti Tun Hussein Onn Malaysia, 86400, Parit Raja, Batu Pahat, Johor, Malaysia
[b] Faculty of Engineering Technology, Universiti Tun Hussein Onn Malaysia, Hab Pendidikan Tinggi Pagoh, Km 1, Jalan Panchor, 84600 Muar, Johor, Malaysia
[c] Faculty of Applied Science and Technology, Universiti Tun Hussein Onn Malaysia, Pagoh Education Hub, 84600 Muar, Johor, Malaysia
[d] NANO-ElecTronic Centre (NET), Faculty of Electrical Engineering, Universiti Teknologi MARA, 40450 Shah Alam, Selangor, Malaysia
[e] Nanotechnology Research Centre, Faculty of Science and Mathematics, Universiti Pendidikan Sultan Idris, 35900 Tanjung Malim, Perak, Malaysia
[f] Department of Engineering, Graduate School of Integrated Science and Technology, Shizuoka University, 432-8011 Hamamatsu, Shizuoka, Japan

ARTICLE INFO

Keywords:
Hydrothermal
Rutile
Ag-FR TiO_2 film
(1 1 0)/(1 1 1) facet
Schottky barrier
Photocatalysis

ABSTRACT

Ag-doped flowerlike rutile-phase (Ag-FR) TiO_2 film with exposed (1 1 0) and (1 1 1) facet was fabricated by a facile hydrothermal method at 150 °C without additive or capping agent with different Ag content ranging from 0.5 to 2 wt%. This study investigated the influence of Ag content in enhancing the photocatalytic activity of Ag-FR TiO_2 film. The flowerlike structures increased the active area of the TiO_2 film. XPS revealed that the concentration of Ti^{3+}-oxygen vacancy defects increased upon doping, while TEM revealed that the (1 1 0) and (1 1 1) are highly exposed facets of rods with flowerlike structure. The effectiveness of the Ag-FR TiO_2 film was tested on methylene blue degradation under xenon lamp irradiation. The Ag-FR TiO_2 film with 1 wt% Ag resulted in the highest methylene blue degradation, which was 20% higher than degradation by the undoped TiO_2. The synergistic effect between both (1 1 0) and (1 1 1) facets and Ti^{3+}-oxygen vacancy from Ag play an important role in reducing the band gap and acts as an electron trap. This suppresses recombination between electrons and holes to enhance the photocatalytic activity thus extending the lifetime of the photogenerated electron and hole.

1. Introduction

The world faces severe water pollution, which affects all living creatures, particularly humans and aquatic organisms. The improper management of waste systems in various industrial settings is one of the sources of hazardous chemicals that affecting global ecosystems. The conventional procedures for eliminating these pollutants have proven to be difficult and ineffective. Hence, this scenario has prompted the introduction of numerous methods such as flotation, membrane process, coagulation, and precipitation to degrade organic compounds [1]. However, these existing methods require improvements to effectively remove the contaminations. Thus, complementary methods have been proposed to remove contaminants for a cleaner environment. In the past few years, advanced oxidation processes (AOPs) have shown great potential for the removal of organic compounds by semiconductor photocatalysis [2]. These processes utilise hydroxyl radicals and superoxide anions to degrade the organic compounds [3].

TiO_2 is a well-known material due to its high chemical stability, high refractive index, large surface area, and cost effectiveness compared to other semiconductors [4–6]. Nevertheless, photocatalysis using TiO_2 is constrained by three major problems: first, the wide band gap of TiO_2 limits its practical environmental application under solar irradiation. Second, the high recombination potential of the photogenerated charge carriers in semiconductors, and lastly, post-separation after the treatment of TiO_2 nanoparticles is a difficult and costly process [7]. Various studies have reported the preparation of powder catalysis in photocatalytic wastewater treatment [8,9]. However, post-separation handling poses a burden in ensuring no powder passes through to the water stream. Thus, the development of film catalysts with comparable photocatalytic activities to the powdered form has emerged to overcome these difficulties.

Generally, many factors contribute to the excellent photocatalytic activity of the film. For example, surface morphology, structural property, surface defect, and fabrication method of the sample [10,11].

* Corresponding author.
E-mail address: akhairul@uthm.edu.my (M.K. Ahmad).

https://doi.org/10.1016/j.apsusc.2020.147571
Received 25 March 2020; Received in revised form 12 August 2020; Accepted 12 August 2020
Available online 15 August 2020
0169-4332/

Table 1
Comparison of studies doped TiO_2 film for MB degradation.

Synthesis method	Dopant type	Percentage degradation (%)	Degradation duration (h)	Ref.
Sol-gel spin coating	Ag	54.13	8	[19],
Thermal oxidation	Au	25	3.5	[25],
Dip coating	Ag	35	5	[26],
Two-step hydrothermal	Pr	76	12	[27],
Hydrothermal method	Ag	75	5	This study

The three main crystallographic forms of TiO_2 are anatase, rutile, and brookite. Each crystalline exhibits a different band gap, surface state, and physical properties. Both anatase and rutile are commonly used in photocatalysis. Many studies have focused on anatase due to its excellent performance in photocatalysis compared to the rutile phase [12]. This may be due to the higher degree of hydroxylation and higher Fermi level in the anatase phase [13]. However, the origin of the low photocatalytic activity of rutile-phase TiO_2 may be due to low surface area from the synthesised route by thermal treatment of the anatase phase at high temperatures (400–1000 °C), which causes aggregation of the catalyst [14]. Furthermore, the rutile phase possesses several advantages over the anatase phase such as high chemical stability and high refractive index [15]. In addition, the rutile phase with rod-like morphology has excellent electron mobility, efficient light-trapping structure, and high surface area that provides more active sites for photocatalytic reaction [16,17]. In another report, Masahashi et al. claimed that the rutile phase ensures higher decomposition of methylene blue (MB) compared to the anatase phase due to high crystallinity, which enhanced the electron mobility in TiO_2 [18].

Moreover, this suggests that the electron transfers to the (1 1 0) facet, while the hole migrates to the (1 1 1) facet that is spatially separated [19]. Therefore, the modification of existing methods is required for a controllable and efficient facet of the catalyst. Hence, dopants are introduced into the lattice TiO_2 by generating local defects such as self-doped Ti^{3+}-oxygen, vacancy in TiO_2, and engineering structural facet. These modifications are widely adopted to increase the performance of TiO_2 in photogenerated carrier transfer and reduce the band gap energy [20]. TiO_2 modification can also be done by introducing metals or nonmetals to produce extra impurity in the energy level that can reduce the band gap energy [21,22].

Among these modifications, self-doped Ti^{3+} is a very attractive additive used to increase the level of impurity. Generally, self-doped Ti^{3+} can be generated by hydrothermal and calcination processes [23], and subsequent treatment by high energy flows such as neutron beam [24], nitrogen-ion implantation [25], and ultraviolet pulsed laser ablation [26]. Moreover, the modification of TiO_2 by metal doping is widely studied. Noble metals such as Au, Ag, and Pt are typically used in the modifications. The metal dopant greatly improves the oxygen vacancy, modifies electron density, and reduces recombination between electron–hole pairs [27].

Ag has a great advantage of lower toxicity, lower cost, and higher antibacterial property compared to Au and Pt, all of which are very useful in wastewater treatment [28,29]. Ag doping is also commonly used to reduce the band gap energy; subsequently, Ag acts as an electron trapper to capture the electrons and react with contaminants [30]. Hence, Ag assists in charge separation by forming a Schottky barrier between TiO_2 and metal [31],[32]. Ag also enhances the absorption of TiO_2 for visible light due to the localised surface plasmon resonance (LSPR). Dong et al. synthesised Ag-decorated TiO_2 nanoparticles to enhance the photovoltaic effect for dye-sensitised solar cell application [33]. The solar conversion efficiency of Ag-decorated nanoparticles is approximately 22% higher than that of undoped TiO_2. Zhou et al. synthesised Ag-decorated Ti^{3+} self-doped porous black TiO_2 pillar using combined oil bath and wet impregnation methods [34]. The authors claimed that the synergistic effect between Ag decoration and Ti^{3+} self-doping enhanced the photocatalytic performance.

To date, many syntheses have been reported in metal-doped fabrications such as sol–gel spin coating [35], solvothermal method [36], electrochemical synthesis [10], and reduction using UV irradiation [37]. However, the abovementioned methods have several drawbacks such as insufficient contact, low efficiency, and extended duration required for sample preparation. In this study, a fast and facile hydrothermal method was designed for the fabrication of Ag-doped rutile-phase TiO_2 film using titanium butoxide ($Ti(OBu)_4$), hydrochloric acid (HCl), deionised (DI) water, and silver nitrate ($AgNO_3$) as a metal dopant at a low temperature of 150 °C for 10 h. No capping agent or toxic additive reagent was used to prevent secondary pollution of the environment. Furthermore, the optimum loading for the doping process was determined from different amounts of the Ag dopants. To the best of the authors' knowledge, limited studies exist on the fabrication of Ag-doped rutile-phase TiO_2 film with active facets (1 1 0), (1 1 1), and Ti^{3+}-oxygen vacancy defects on fluorine-doped tin oxide (FTO) substrate using a simple hydrothermal method. Table 1 shows a comparative summary of previous works and the current study on MB degradation.

2. Experimental

2.1. Materials and methods

Hydrochloric acid (HCl) was purchased from J. T. Baker with 36–38% purity. Titanium(IV) butoxide ($Ti(OBu)_4$) and fluorine-doped tin oxide (FTO) substrates were purchased from Sigma-Aldrich. Methylene blue (MB) was purchased from Wako. Silver nitrate ($AgNO_3$) was purchased from QRëC. All chemicals were used without any purification.

2.2. Preparation of Ag-FR TiO_2 film

Fig. 1 shows the schematic illustration of the fabrication route for the Ag-FR TiO_2 film. The Ag-FR TiO_2 film was fabricated using a simple one-step hydrothermal method. The FTO substrate was cut into 35 × 35 mm dimensions before cleaning with acetone, ethanol, and DI water using the sonication method. Precisely, 80 mL of HCl was mixed with 80 mL of DI water and stirred for 5 min in a clean beaker. Next, the mixed solution was heated to 212 °C. Then, $AgNO_3$ was added into the solution at different weight percentages and the solution was stirred for 30 min. The solution was subsequently cooled to room temperature. Then, 0.10 M of $Ti(OBu)_4$ was added dropwise, and the mixture was stirred until the solution was clear.

The FTO substrate was placed in the conductive area facing upward. Then, the prepared solution was poured into a steel autoclave with Teflon liner (300 mL). The hydrothermal reaction was conducted for 10 h at 150 °C. After cooling down, the film was rinsed several times in DI water and dried in the oven at 100 °C for 30 min. No post-annealing treatment was applied. The films were denoted as TiO_2 (undoped TiO_2), TiO_2—Ag 0.5 wt%, TiO_2—Ag 1.0 wt%, and TiO_2—Ag 2.0 wt% according to the weight percentages of the dopant.

2.3. Characterization of Ag-FR TiO_2 film

The X-ray diffraction (XRD) PANalytical X-Pert Powder machine was used to examine the structural properties of the film at 2θ from 20°

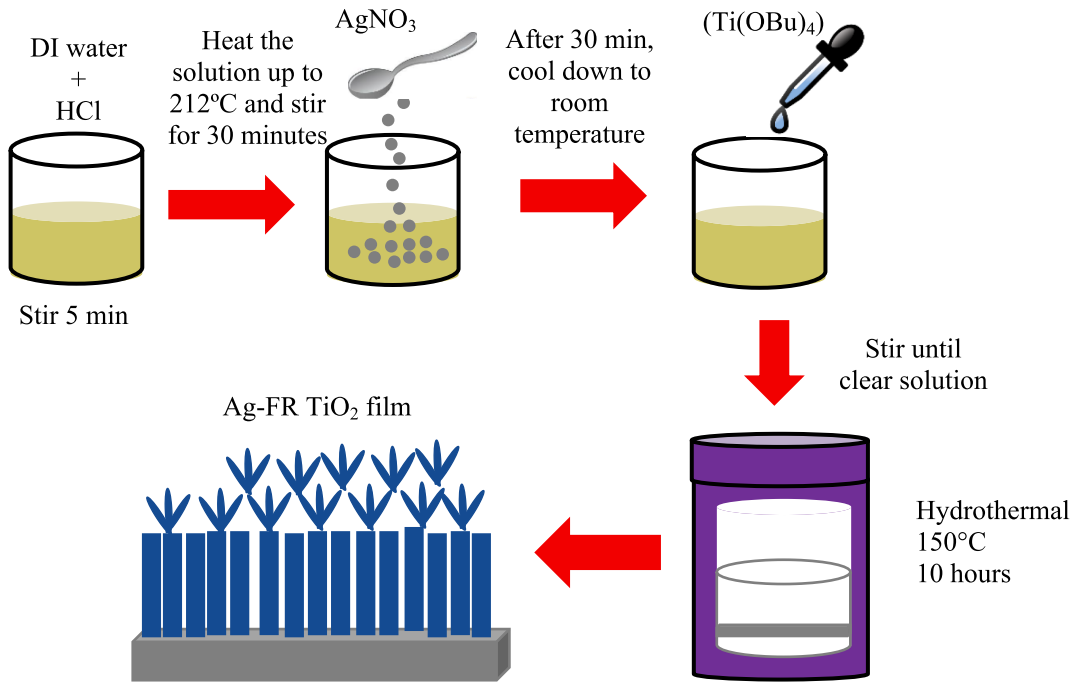

Fig. 1. Schematic illustration of the fabrication route for making Ag-FR TiO_2 film.

to 80°. Raman spectroscopy (XploRA PLUS model BX41TF) was used to further examine the structural property. FESEM JEOL JSM-7600F was used to study the surface morphologies and the elemental property of the samples. The electron energy used for EDX analysis was 15 kV. Transmission electron microscopy (TEM) model JEOL JEM-2100F was used to observe the lattice fringes and shape of the films. Photoluminescence spectroscopy (Jasco spectrofluorometer FP-8600) was used to analyse the characteristics of the light emitted from the photo-excited materials. UV–vis NIR spectroscopy (Shimadzu 3600 Plus spectrophotometer) was used to examine the optical property of the film. XPS spectroscopy (AXIS ultra) was utilised to investigate the defect levels in TiO_2.

2.4. Photodegradation of MB

The ability of the rutile-phase TiO_2 film in photocatalytic activity was tested for MB degradation using a xenon lamp (MAX-303, Asahi spectra, 300 W), which has a wide wavelength ranging from 300 to 600 nm. The power density of the xenon lamp was 20 mW cm^{-2}. Fig. 2 shows an illustration of the photodegradation of MB. The rutile-phase TiO_2 film was placed in the beaker. The distance of the lamp to the solution was 21 cm. Then, the film was exposed to light for 30 min to eliminate unwanted adsorption of molecules and to enhance the adsorption of MB on the TiO_2 surface. Next, 100 mL of MB solution was poured and stirred in the dark for 1 h to attain adsorption–desorption equilibrium. The initial pH of the solution was 12, while the initial concentration of MB was 5 mg/L. At least three replicate experiments were conducted to confirm the reproducibility. The experiment was continued for 5 h with continuous stirring during which 3 mL of the sample was collected at 1 h intervals. The dye degradation was calculated using Eq. (1).

$$\text{Dye degradation } (\%) = \frac{A_o - A_t}{A_o} \times 100 \quad (1)$$

where A_o is the initial absorbance and A_t is the absorbance at a time, t. The absorption of MB was taken at 664 nm.

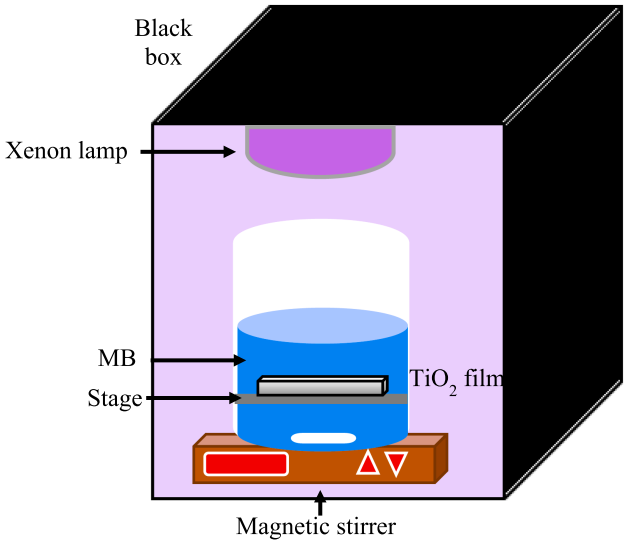

Fig. 2. Schematic diagram for Photodegradation of MB.

3. Results and discussion

3.1. Structural analysis

The XRD analysis was performed to investigate the structural properties of the films in the range of 20–80°, as shown in Fig. 3(a). All the samples show peaks for the rutile phase, whereas no anatase peak was detected. The XRD peak detected matched the JCPDS file No: 98-008-0842. The XRD patterns obtained from the analyses showed that pure rutile phase was formed from the simple hydrothermal method without calcination. The peaks at 2θ of 27.38°, 36.10°, 41.24°, and 54.5° fitted well with the (1 1 0), (1 0 1), (1 1 1), and (2 1 1) planes of the rutile phase of TiO_2, respectively [38]. The Ag-FR TiO_2 film is crystalline even without thermal treatment. No diffraction peak for Ag or its oxides was detected, which confirms that the rutile phase was not interrupted upon doping. This finding reveals that silver ions were successfully dispersed on the TiO_2 matrix. This also agrees with a previous study where XRD

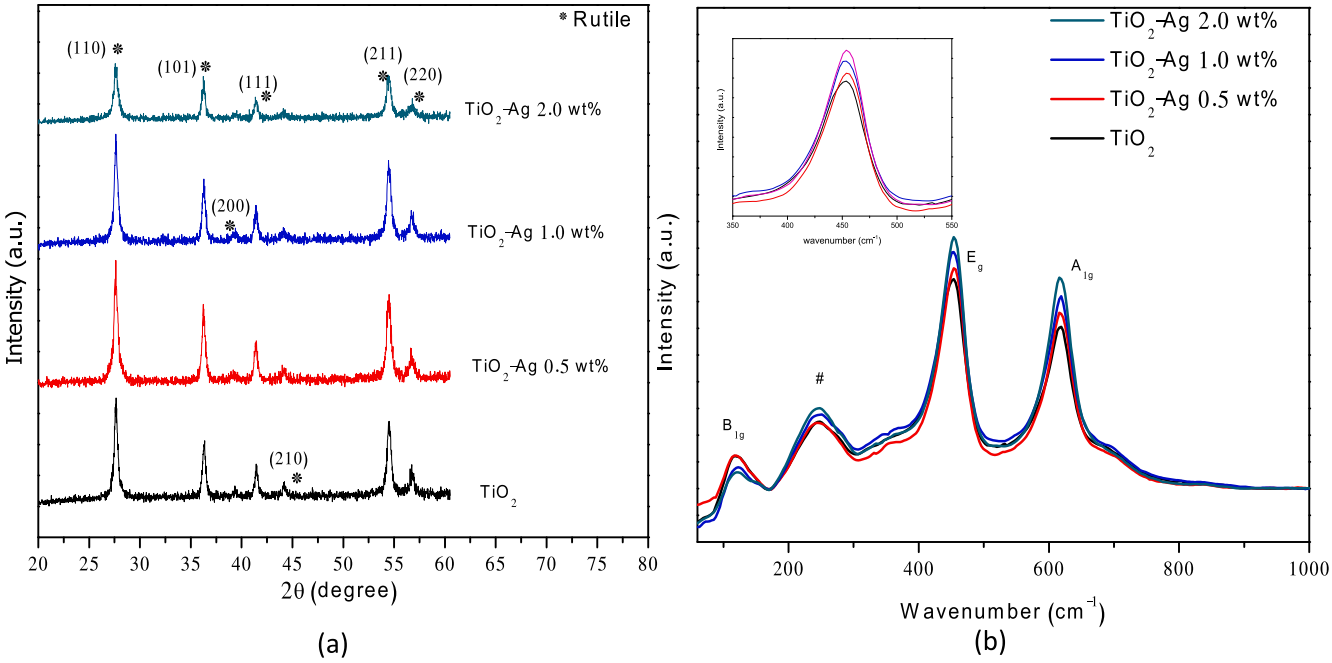

Fig. 3. (a) XRD spectra (b) Raman shift for undoped TiO_2 and various amount of Ag dopant.

analysis was unable to detect Ag, particularly if the Ag content is < 4 wt% [39]. Hence, the deposited Ag is expected to be lower than the visibility limit for XRD [40].

At high dopant concentration, the intensity of the peaks decreased. This observation may be due to the incorporation of Ag ions into the parent lattice of TiO_2, which resulted in modification of the lattice's periodicity and crystal symmetry [33]. The data also show that the diffraction peak slightly shifted to the lower angle values, which can be explained by the ionic radius of the incorporated metal ion in the TiO_2 lattice. The diffraction peak of the XRD spectra is shifted to a lower angle due to the incorporation of the metal ion with a larger radius, while a smaller ionic radius will shift the XRD spectra to the higher angle [41]. It is well known that the rutile phase has good electron mobility, which helps the electron move to the surface and react with the wastewater [42]. The crystallite size of the Ag-FR TiO_2 film was calculated using the Debye–Scherrer equation at the major peak of the rutile phase at $2\theta = 27.38^{\circ}$ (Eq. (2)).

$$D = \frac{k\lambda}{\beta}cos\theta \quad (2)$$

where D is the crystallite size, k is the shape factor ($k = 0.94$), λ is the wavelength of the X-ray radiation (Cu Kα = 0.1542 nm), β is the full width at half maximum (FWHM), and θ is the angular position of maximum peaks location. The crystallite size ranges from 33 to 86 nm as shown in Table 2 but decreased with the increase in Ag content. The presence of Ag ions leads to the repulsion between the Ti ions, which may possibly inhibit crystal growth and result in smaller particle size. This result is coherent with a previous study by Ali et al. [30].

Raman spectroscopy was conducted for further investigation of structural properties of the Ag-FR TiO_2 film. The rutile phase was depicted by a tetragonal space group of P42/MM, which has four main transitions including B_{1g}, multi proton process (#), E_g, and A_{1g} [13]. The Raman spectra of the pristine TiO_2 and Ag-FR TiO_2 films with different Ag concentration are shown in Fig. 3(b). All the peaks shown represent the Raman shifts for the rutile phase [43]. These results have good agreement with the XRD result. The Ag-FR TiO_2 film shows good crystallinity even without annealing treatment. The Ag-FR TiO_2 film has a pure rutile phase crystal but no Ag peak exists in the result. The sample displays the main peaks at 120 cm^{-1} (B_{1g}), 244 cm^{-1} (multi-proton process), 453 cm^{-1} (E_g), and 622 cm^{-1} (A_{1g}). The E_g mode is due to the symmetric stretching vibration of O—Ti—O, while the B_{1g} mode is from symmetric bending vibration of O—Ti—O, and A_{1g} is from anti-symmetric bending vibration of O—Ti—O [44]. Fig. 3(b) shows that the 453 cm^{-1} (E_g) peak slightly shifted towards a higher wavelength when the Ag concentration increased.

Generally, the shift in Raman peak may be due to the modifications or defects in the structure and changes in particle size [30]. The peaks broadened when the Ag concentration increased, which can be correlated to the increase in oxygen vacancy concentration on the Ag-FR TiO_2 film [45]. Another reason for the broadening of the peak may be due to the effect of particle size on the force constant and vibrational amplitude [30]. In Table 2, the A_{1g} intensity ratio to E_g was compared. At higher Ag concentrations, the stretching of the A_{1g} peak was affected by the replacement of Ti atoms by Ag atoms. This phenomenon shows the increasing intensity ratio of the A_{1g}/B_{1g} modes and proves that the Ag dopant was successfully incorporated into the TiO_2 structure.

Table 2
FWHM, Crystallite size (D) and Raman percentage of different Ag concentrations.

Sample	β (FWHM)	D (nm)	Raman A_{1g}/E_g (%)
TiO_2	0.1968	86.86	77.8
TiO_2-Ag 0.5 wt%	0.416	41.09	87.41
TiO_2-Ag 1.0 wt%	0.4305	39.71	91.45
TiO_2-Ag 2.0 wt%	0.511	33.45	93.89

3.2. Morphology

Fig. 4 shows the surface morphology of the fabricated undoped TiO_2 and TiO_2—Ag 1.0 wt%. The sample displays a flowerlike structure containing a bundle of the rods. The flower distribution covered on top of the FTO structure. The average diameter of a single rod of the flower is from 90 to 120 nm, while the average diameter of the flower is from 7 to 9 μm. The 3D microstructure significantly contributes to the large surface area, whereas the multiple petal arms provide more active sites for the photocatalytic activity that enhances MB photodegradation. The charge transportation between the electron and the hole in the rod's

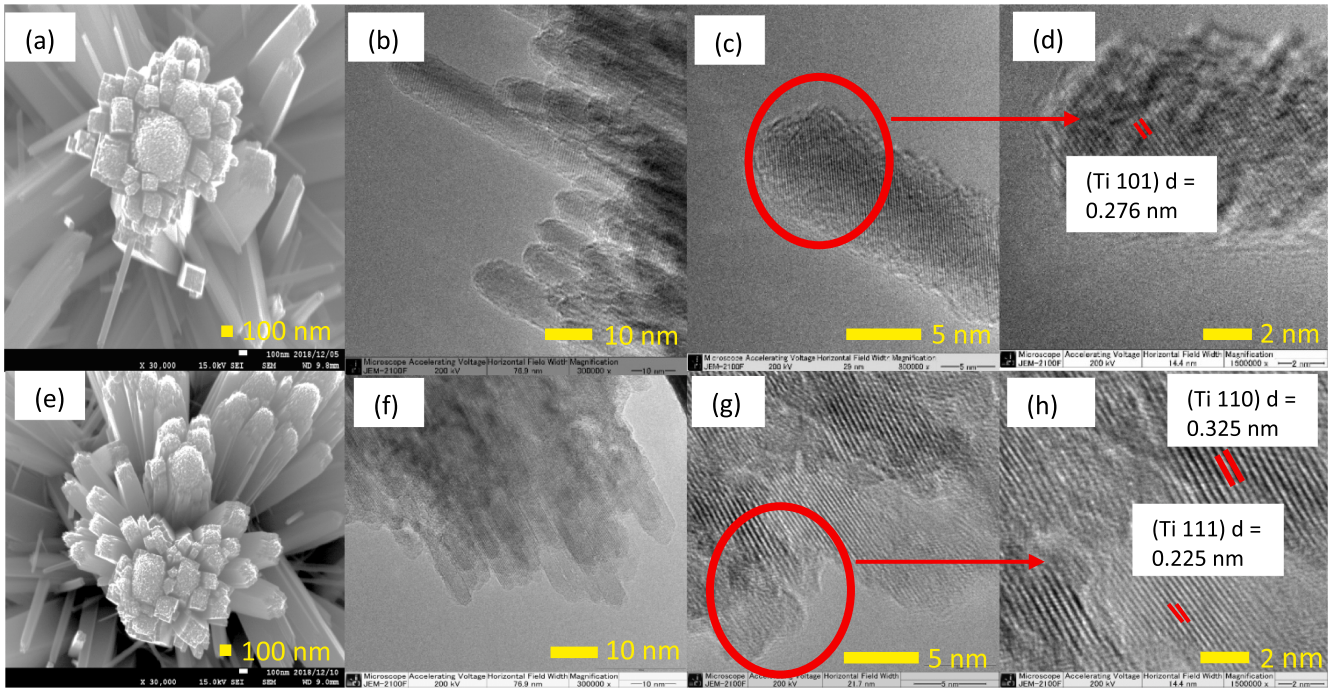

Fig. 4. (a) FESEM image for undoped TiO_2, (b–d) HR-TEM images for undoped TiO_2, (e) FESEM image for TiO_2—Ag 1.0 wt% film, (f–h) HR-TEM images for TiO_2—Ag 1.0 wt% film.

structure was also improved by localising the electron in the direction along the crystal length. Though the nanopore offers a high surface-to-volume ratio, it cannot ensure efficient transportation of the charge carrier due to the multiple paths and hence traps the electron at the grain boundaries [16]. Thus, the morphology of the flowerlike structure containing the rod petal offers a direct pathway for the electron to overcome the recombination between electron and hole.

Fig. 4(b) and (f) show the petal arrangement of the rods for both samples, which also consists of fine rods. The size of the fine rods can clearly be seen in the HR-TEM result. From Fig. 4(d) of the undoped TiO_2, the exposed facet is at (101) with a lattice fringe value of 0.276 nm, which is a match with the XRD data. This finding contradicts a previous study which claims that the exposed facet for the rutile phase is at (110) [11]. Fig. 4(f) to (h) show the HR-TEM images of the TiO_2—Ag 1.0 wt% film and the lattice fringes of 0.325 and 0.225 nm corresponding to (110) and (111) facets, respectively. The fine rods' sizes range from 7 to 10 nm. For the rutile phase, rutile (110) and (111) have been reported to act as active photocatalytic sites [46]. These high-energy facets enhance photocatalytic activity. The lattice arrangement of the doped sample changed, which proves the ability of Ag dopant to modify the TiO_2 lattice. The combination between the (110) and (111) facets also induced the spatial separation between electron and hole pairs [19]. Fig. 5(a) shows the elemental mapping Ti, O, and Ag in the TiO_2—Ag 1.0 wt% film. It shows that the Ti, O, and Ag elements are uniformly distributed in the Ag-FR TiO_2 film. However, from the EDX spectrum analysis, Ag element was not detected even with 15 keV of electron beam energy (Figure (b)). This may due to the low weight percentage of dopant used in the doping process. In addition, when mapping a surface area with high roughness, there is a high possibility of elemental peak overlapping that may cause misinterpretation of a simple X-ray, due to low reflection from a surface. Thus, we further clarified the detection of Ag element through XPS analysis in Section 3.5. The proposed growth mechanism of flowerlike rutile-phase TiO_2 film is described in Eqs. (3) and (4) [47],:

$$Ti(C_3H_7O)_4 + 4H_2O \rightarrow Ti(OH)_4 + 4C_3H_7OH \text{ (hydrolysis)} \quad (3)$$

$$Ti(OH)_4 \rightarrow TiO_2 + 2H_2O \text{ (condensation)} \quad (4)$$

At the first step, tetrabutyl titanate was hydrolysed to form $Ti(OH)_4$ (Eq. (3)). This was followed by the formation of the octahedral TiO_6 from the protonation of the OH ligands by HCl, and subsequently, the condensation of $Ti(OH)_4$ which leads to the formation of the 3D structure of TiO_2 [48,49] (Eq. (4)). The rutile phase was reportedly formed under the high acidic condition when HCl was used to control the hydrolysis process [50]. HCl plays a significant role in producing the rod-like structure of rutile TiO_2. The formation of rutile TiO_2 is based on the edge-sharing mode. Furthermore, the Cl^- affects the orientation along the *c* direction. The (110) plane that possesses a polar surface and Cl^- restricts formation in the [110] direction and growth along the [001] direction [51]. The accelerated growth in the [001] direction leads to the formation of a rod-like structure.

For the flower structure, the grain growth from the crystal nuclei formed in the solution tends to tilt from the original nucleation centre of the (110) plane and grows identically along the [001] direction; hence, it produces multi-arm rods that are similar to the flowerlike structure [52]. If the condensation process is increased, the formation of oxygen vacancy is also increased, and hence, the electron trapped at Ti^{4+} will form Ti^{3+} [53]. Fig. 6 shows the difference between the sample growth of the undoped TiO_2 and the Ag-FR TiO_2 film. Oliver et al. calculated the surface energy for rutile and found the lowest energy in the (110) faces, followed by (101) and (001) surfaces [54]. It is proposed that the lower surface energy of the crystallographic face has a higher affinity for its attachment orientation. This phenomenon will lead to the attraction of Ag to attach to the lower surface energy of the crystal face, which are the (110) faces. The introduction of Ag dopant changed the TiO_6 octahedral chain. The Ag dopant induced fewer surface defects at the edge and more surface defects at the face of TiO_6 octahedral. Thus, the decrease in the lattice size increased the density of the TiO_2 flower petal, and Ag was well dispersed in TiO_2.

3.3. Optical property

Fig. 7(a) shows the diffused reflectance spectra with different Ag contents of 0.5 to 2.0 wt% and undoped TiO_2 film. The results show that both the undoped TiO_2 film and Ag-FR TiO_2 films have a strong

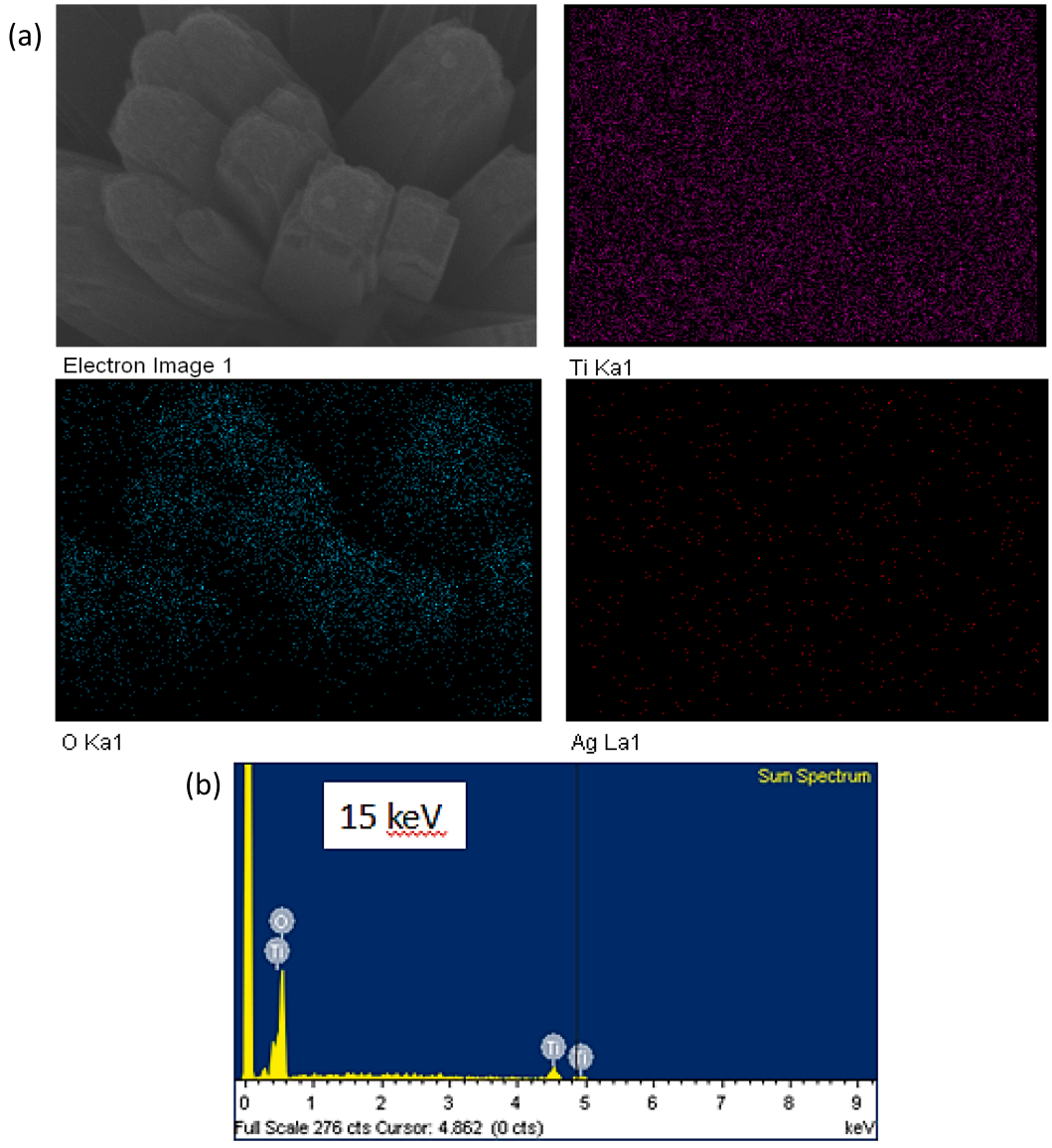

Fig. 5. (a) Elemental mapping (b) EDX spectrum for TiO_2—Ag 1.0 wt% sample.

absorption for ultraviolet spectrum. The reflectance percentage decreased with increasing Ag content. This may be due to the existence of the Ag dopant and Ti^{3+}-oxygen vacancy defects in TiO_2. Fig. 7(b)–(e) show the band gap for the undoped TiO_2 film and Ag-FR film. The diffuse reflectance spectra were converted into the Kubelka–Munk function [F(R)] for band gap calculation, which is based on Eq. (5).

$$F(R) = +\frac{(1-R)^2}{2R} \tag{5}$$

where R is the reflectance. The band gap was obtained from the modified Kubelka–Munk function versus the energy of the absorbed photons graph, $[F(R) \times h\nu\ ]^n$ [55]. The pure TiO_2 film has 3.21 eV, while the Ag-FR film was reduced to 3.18 eV for 0.5 wt%, 3.12 eV for 1.0 wt%, and 3.06 eV for 2.0 wt% of Ag. This shows the synergistic effect of the Ag dopant, and that the Ti^{3+}-oxygen vacancy defect is responsible for reducing the band gap and introducing intermediate levels that require less energy for electron excitation. It is expected that this behaviour will significantly assist in enhancing the photocatalytic activity of the Ag-FR TiO_2 film.

3.4. Photoluminescence (PL) analysis

The PL analysis examines the effectiveness of charge carrier trapping, transfer, and immigration of an electron, and the intermediate level or shallow trap in the semiconductors. Fig. 8(a) shows the PL spectra for the undoped TiO_2 film at various contents of the Ag-FR TiO_2 film with an excitation wavelength of 300 nm. Three strong emission peaks are shown at 423, 468, and 651 nm. The 423 nm excitation is attributed to the near band edge of the estimated band gap of TiO_2 [56]. Other emission peaks observed may be due to surface-state emissions. The surface state is a shallow trap near the absorption band edge located within the band gap of the catalyst and acts as an electron trap that can cause emission at higher wavelength [57]. The emission peaks at 1.90 eV are due to the Ti^{3+}-oxygen vacancy defect state, which is located between 0.7 and 1.0 eV below the conduction band [58],[59]. Moreover, the shoulder peak beside the main peak may be due to the Ti^{2+} defect, which is explained later in chemical state analyses. This result agrees with the band gap energy calculation by the Kubelka–Munk equation, which indicates that the Ag dopant and Ti^{3+}-oxygen vacancy defects help to create the surface defect state and hence, reduces the band gap energy.

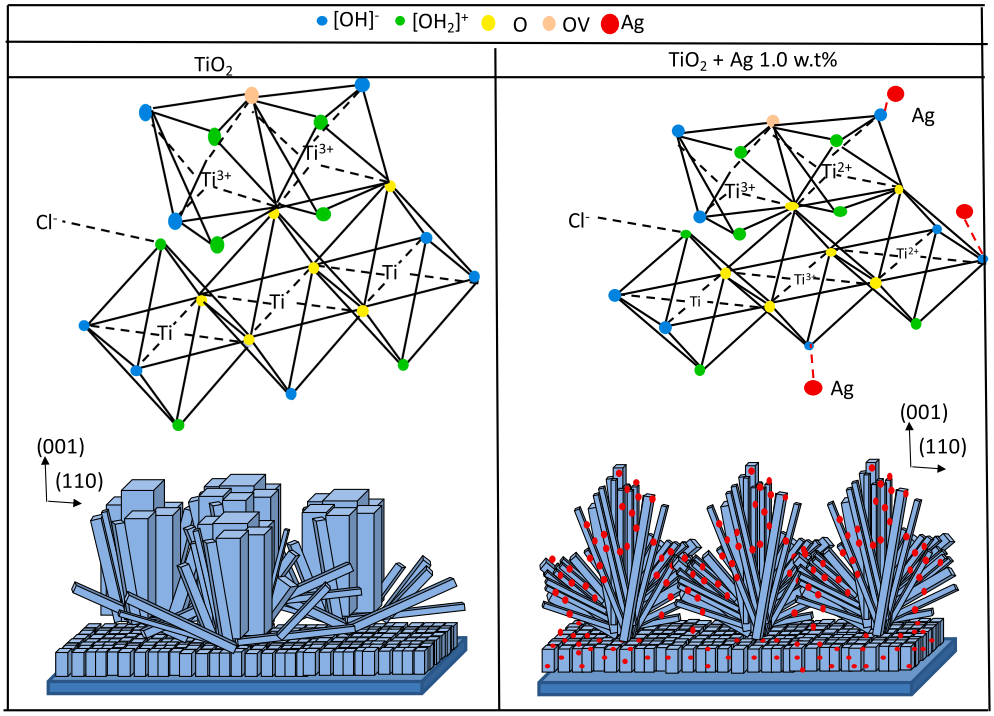

Fig. 6. Difference between sample growth of undoped TiO_2 and Ag-FR TiO_2 film.

Fig. 8(b) shows the illustration of the PL mechanism affected by the defect state that reduces the band gap energy. The PL spectra exhibit a similar pattern between the undoped TiO_2 and Ag-FR films but with different intensities of PL. The lower intensities of the PL spectra indicate the suppression of electron recombination between holes at the valence band in the TiO_2 film. This phenomenon is verified at optimum Ag content, which is the TiO_2—Ag 1.0 wt% film. It has the lowest intensity of PL spectra and successfully delays the recombination between the electron and hole pair. This gives more time for the electron and holes to react with the contaminants. Moreover, the Schottky barrier also suppressed the recombination between the electron–hole pair, in which the Ag dopant acts as an electron trapper to avoid the electron

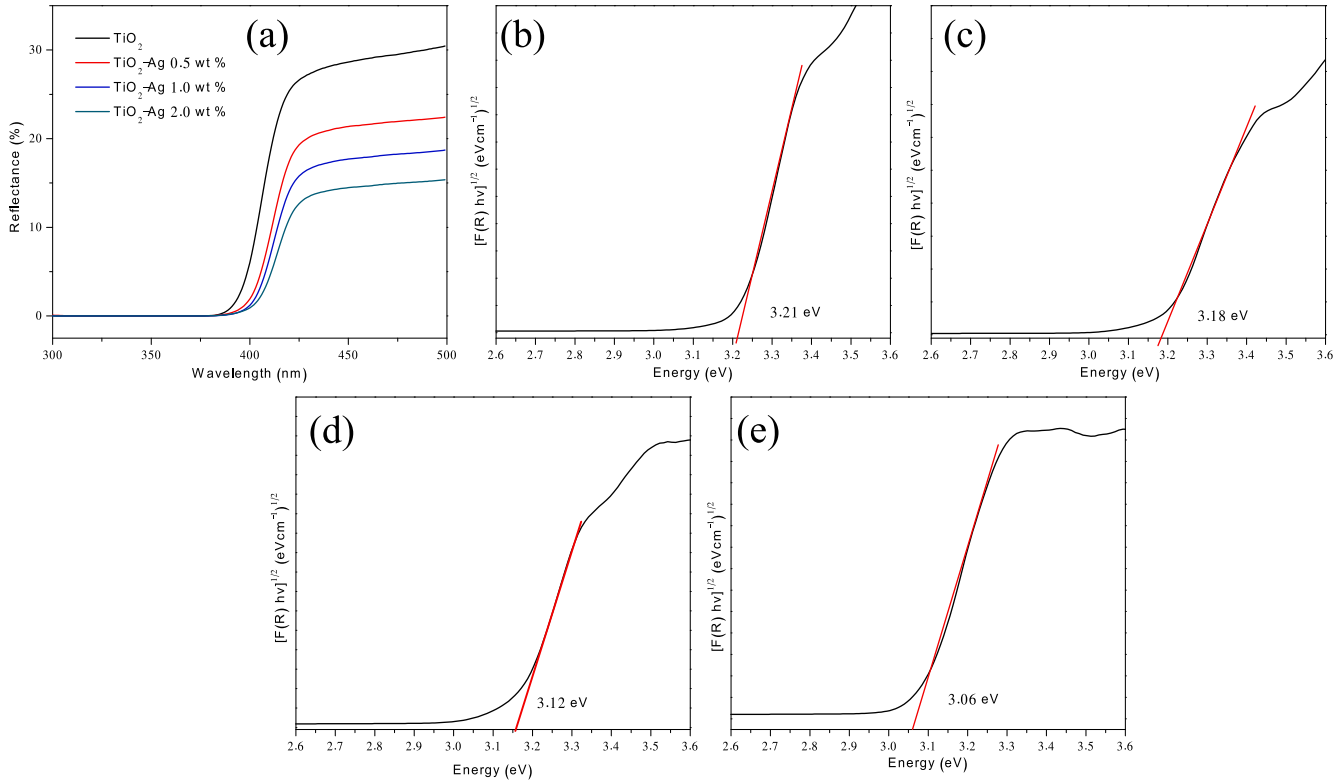

Fig. 7. (a) Reflectance spectra, Estimation band gap energy from Kulbeka Munk equation (b) undoped TiO_2 (c) TiO_2-Ag 0.5 wt% (d) TiO_2-Ag 1.0 wt% (e) TiO_2-Ag 2.0 wt%

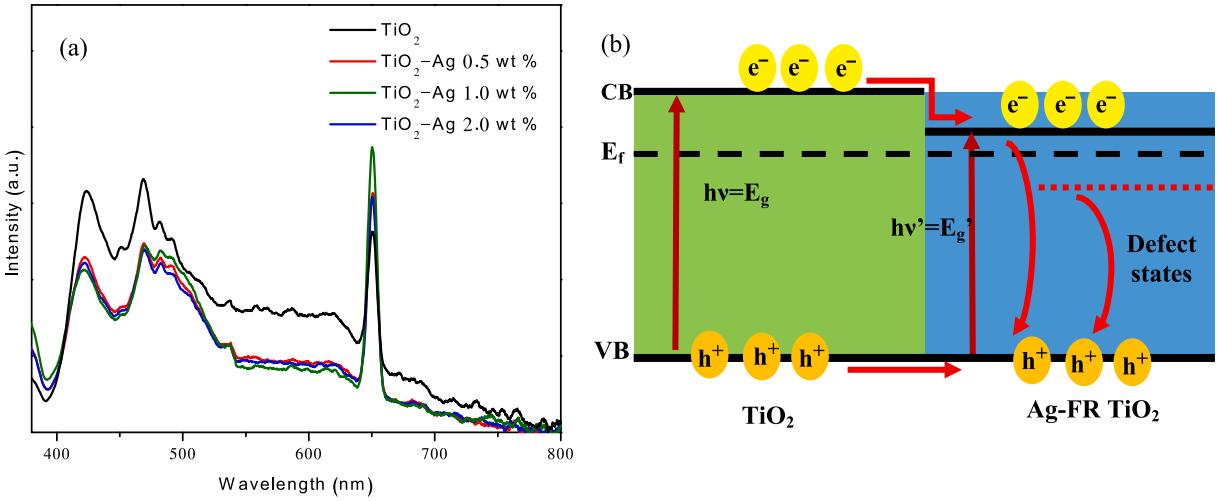

Fig. 8. (a) PL spectra of undoped TiO_2 at various amounts of Ag dopant, (b) The illustration of the PL mechanism by defect states.

from back-transferring to TiO_2 [60]. These synergistic effects between the Ti^{3+}-oxygen vacancy defect and the Schottky barrier are strongly responsible for enhancing the photocatalytic activity compared to the pure flowerlike rutile-phase TiO_2 film.

3.5. Chemical state analysis

The surface chemical state was investigated using X-ray photoelectron spectroscopy (XPS). For TiO_2, the oxygen vacancy was formed from the surface defects, where the Ti^{4+} was reduced to lower oxidation states such as Ti^{+}, Ti^{2+}, and Ti^{3+}, thus acting as an electron trap to suppress the recombination between the electron–hole pairs [24]. Generally, these defects can be generated by Ti^{4+} reduction. When the Ti^{4+} ions accept the electron while being exposed to UV irradiation on the TiO_2 catalyst, the formation of Ti^{3+} occurs. The electron was trapped to reduce Ti^{4+} to Ti^{3+}, while the hole oxidises the O^{2-} anions to the hole trapped (O^{-}) [61]. This electron trap enhances the photocatalytic activity.

Fig. 9 shows the de-convolution spectra of the narrow scan XPS spectra for Ti 2p and O 1s for the undoped TiO_2 and the TiO_2—Ag 1.0 wt % sample. Table 3 presents a summary of the binding energy value for the undoped TiO_2 and Ag-FR TiO_2 film from XPS analysis. A carbon correction was applied at 284.6 eV on the high-resolution scan. For the undoped TiO_2 (Fig. 9a[i]), the Ti 2p consists of two spin orbitals at 458.86 and 464.56 eV, which correspond to the Ti^{4+} $2p_{3/2}$ and Ti^{4+} $2p_{1/2}$, respectively with a binding energy difference of 5.72 eV. Furthermore, the Ti^{3+} defect already exists in the undoped TiO_2 sample, which proves that the hydrothermal method has the ability to produce the defects. The shoulder peaks at 457.18 and 462.88 eV represent Ti^{3+} $2p_{3/2}$ and Ti^{3+} $2p_{1/2}$ with a binding energy difference of about 5.70 eV, which is similar to the previous study [62].

When compared to the TiO_2—Ag 1.0 wt% sample (Fig. 9b[i]), the Ti 2p peak shifted to lower binding energy, and the peak broadened. This is due to the decrease in Ti^{4+} and the increase in Ti^{3+} and Ti^{2+} oxidation states, which exist after doping with Ag as shown in Fig. 9. This proves the successful doping of Ag into the TiO_2 lattice. This high-resolution scan is well-fitted by the Gaussian–Lorentzian fitting with the energy centred at 458.59 and 464.29 eV of Ti^{4+} $2p_{3/2}$ and Ti^{4+} $2p_{1/2}$, respectively. The Ti^{3+} oxidation state for the TiO_2—Ag 1.0 wt% sample located at 457.39 and 463.09 eV correspond to Ti^{3+} $2p_{3/2}$ and Ti^{3+} $2p_{1/2}$, respectively. The Ti^{2+} oxidation state also appeared in this sample at 455.36 eV and 461.06 eV with a difference of 5.70 eV binding energy. The existence of Ti^{2+} was also confirmed by the PL analysis.

The shoulder peak arises beside the major peak, which means there has been an electron and hole recombination. In addition, the area under the graph represents the concentration of that element. The Ag dopant was triggered to produce a higher concentration of Ti^{3+} and Ti^{2+}, resulting in decreased Ti^{4+} concentration. The concentration of the Ti^{3+} $2p_{3/2}$ (65.32%) of the undoped TiO_2 decreased to 22.57% for the TiO_2—Ag 1.0 wt% sample. Table 4 shows the summarised data for the intensity ratios of Ti^{4+}/ Ti^{3+} and Ti^{3+}/Ti^{2+} for the undoped TiO_2 and TiO_2—Ag 1.0 wt% film. The results show that the intensity ratio of Ti^{4+}/ Ti^{3+} decreased after the doping process and an increase in the Ti^{3+}/Ti^{2+} intensity ratio. The presence of the Ag dopant in this reaction introduces an oxidation state into the TiO_2 catalyst, which acts as an electron trap, delaying the recombination between the electron–hole pair and thus enhancing the photocatalytic activity. This data was correlated with PL characterisation, which shows several peaks that proved the existence of the oxidation state in the film.

Fig. 9a(ii) and b(ii) show the high-resolution scans of the O 1s peak for the undoped TiO_2 and doped sample for TiO_2—Ag 1.0 wt%, respectively. The undoped TiO_2 sample consists of two major peaks centred at 530.06 and 531.57 eV, which are attributed to the lattice (O_L) and hydroxyl (O_H), which is similar to the output of a previous study [27]. In the TiO_2—Ag 1.0 wt%, the O 1s peak became wider and produced an additional peak centred at 530.19 eV. This peak is attributed to bridging (O_B) binding energy. This bridging binding energy correlates to the connection between the Ag—O bonds. This proves that the dopant has successfully entered the lattice of TiO_2.

The $3d_{5/2}$ and Ag $3d_{3/2}$ peaks for the Ag dopant are centred at 366.9 and 372.9 eV, respectively as shown in Fig. 10. The splitting of the 3d doublet with a 6 eV difference in binding energy proves the presence of Ag in the TiO_2—Ag 1.0 wt% film in the form of metallic Ag [63]. The high interaction between Ag and the defective site of TiO_2 causes the forceful transfer of an electron to the Ag metal. This effective interfacial interaction is needed for electron trapping and hence, enhances the photocatalytic performance.

3.6. Photodegradation of MB

The effectiveness of the Ag-FR TiO_2 film and the undoped TiO_2 film was evaluated by MB degradation. To ensure the reproducibility of the results, the photocatalytic reactions were carried out in triplicates. The replication of degradation data was within the 95% confidence limit as tabulated in Table 5. Fig. 11(a) shows the photodegradation of MB by pure TiO_2 film and Ag-FR TiO_2 film with various Ag content under xenon lamp. The initial pH of the MB solution was set at 12 to ensure the MB degrades continuously during the entire irradiation time for all films. The TiO_2-Ag 1.0 wt% film showed the highest MB degradation at 75% within 5 h followed by TiO_2—Ag 0.5 wt% film and TiO_2—Ag 2.0 wt

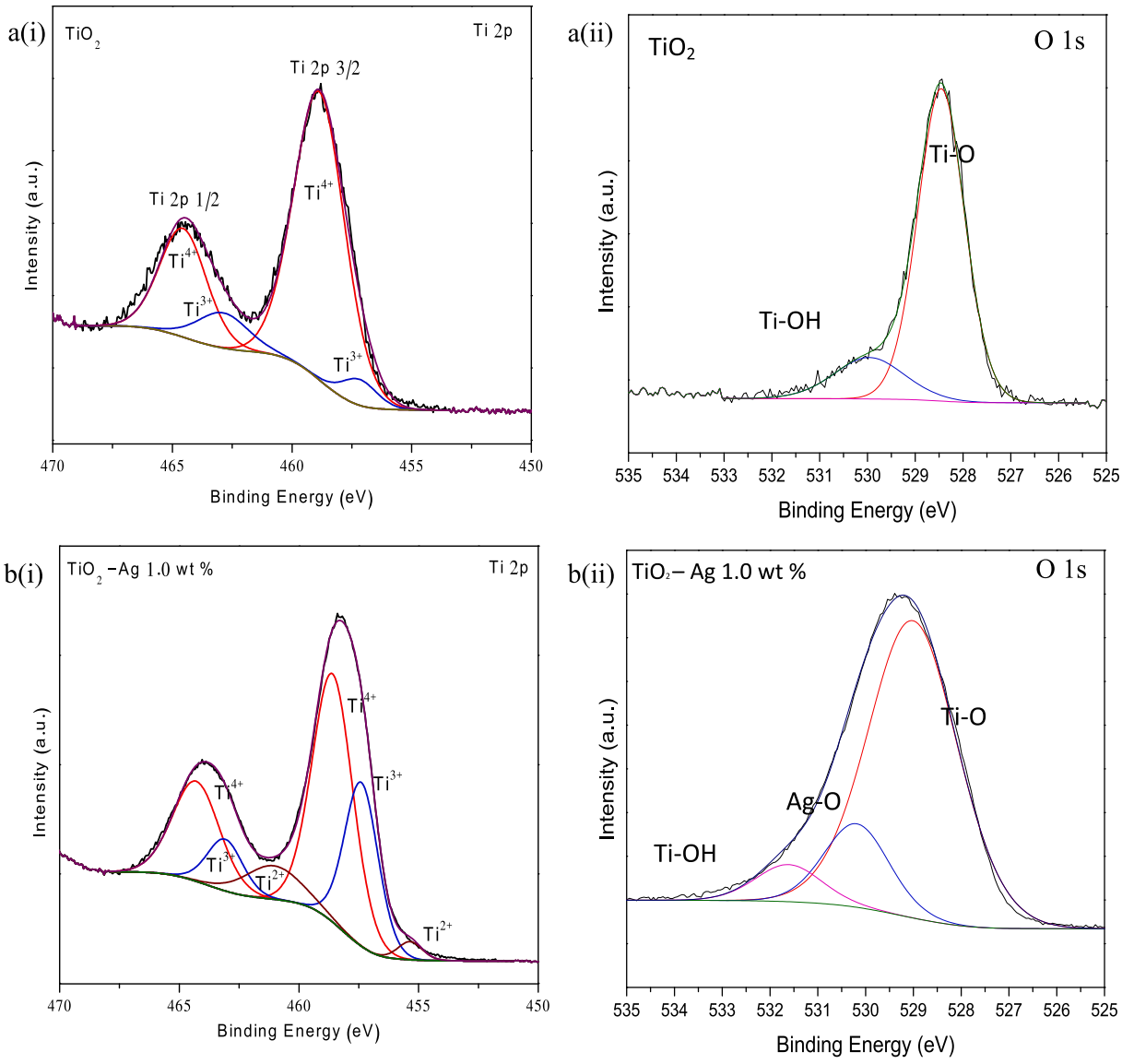

Fig. 9. a(i–ii) Ti 2p and O1s deconvolution graph for undoped TiO_2, b(i–ii) Ti 2p and O 1s deconvolution graph of TiO_2-Ag 1.0 wt%.

% film with 67% and 64%, respectively. The pure TiO_2 film showed the lowest degradation of MB at only 59%. High Ag content lowered the efficiency of the photodegradation process. Thus, the 1.0 wt% loading of Ag represents the optimum loading for enhanced photodegradation of MB. Fig. 11(b) shows the kinetics study for the undoped TiO_2 and Ag-FR TiO_2 film with various Ag content. The photodegradation reaction rate constant (k) was calculated by re-plotting the photodegradation ratio according to the pseudo-first-order reaction as given in Eq. (6) [64],:

$$\ln C_o/C_t = k_t \quad (6)$$

Table 4
Ratio of Ti^{4+}/Ti^{3+} and Ti^{3+}/Ti^{2+} for undoped TiO_2 and TiO_2-Ag 1.0 wt% film.

Sample	Ti $2p_{3/2}$		Ti $2p_{1/2}$	
	Ti^{4+}/Ti^{3+}	Ti^{3+}/Ti^{2+}	Ti^{4+}/Ti^{3+}	Ti^{3+}/Ti^{2+}
TiO_2	5.69	nil	1.68	nil
TiO_2-Ag 1.0 wt%	1.53	4.77	1.40	1.23

Table 3
Binding energy value for undoped TiO_2 and Ag-FR TiO_2 film from XPS analysis.

Samples	Ti 2p (eV)						O 1s (eV)			Ag 3d (eV)	
	$2p_{3/2}$			$2p_{1/2}$			Ti—O	Ag—O	OH	3d5/2	3d3/2
	Ti^{4+}	Ti^{3+}	Ti^{2+}	Ti^{4+}	Ti^{3+}	Ti^{2+}					
TiO_2	458.86	457.18	nil	464.56	462.88	nil	530.06	nil	531.57	nil	nil
TiO_2-Ag 1.0 wt%	458.59	457.39	455.36	464.29	463.09	461.06	529.01	530.19	531.61	399.9	372.9

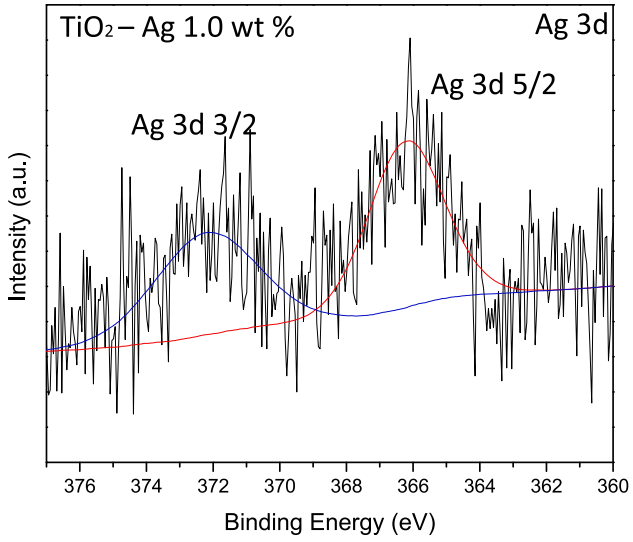

Fig. 10. Ag 3d deconvolution graph for TiO_2-Ag1.0 wt%.

Table 5
Dye degradation and k_{app} value for various Ag weight percent. The degradation correspond to 95% confidence limit.

Samples (wt%)	Dye degradation (%)	$K_{app}(\times 10^{-2}\ min^{-1})$	R^2 value
TiO_2	59 ± 1.67	0.183	0.9974
TiO_2-Ag 0.5 wt%	67 ± 2.83	0.376	0.9996
TiO_2-Ag 1.0 wt%	75 ± 2.90	0.464	0.9983
TiO_2-Ag 2.0 wt%	64 ± 1.20	0.342	0.9974

where C_o and C_t are the maximum absorbance of the MB at initial time and time t, respectively.

The summarised data on the percentage degradation, rate constant (k), and regression rate (R) are shown in Table 5. The K value increased from 0.183×10^{-2} to $0.464 \times 10^{-2}\ min^{-1}$ for pure TiO_2 film and TiO_2—Ag 1.0 wt%, respectively. The K value decreased to $0.342 \times 10^{-2}\ min^{-1}$ for TiO_2—Ag 2.0 wt%. These results suggest that the TiO_2 modification with the Ag metal successfully enhanced the photodegradation of MB. Generally, many factors contribute to the excellent photocatalytic activity of the film, for example, surface morphology, structural property, surface defect, and the fabrication method of sample, among others [10,11].

The flowerlike morphology provides numerous active sites for the photodegradation of MB. In addition, the flowerlike morphology has a scattering effect that helps the photon disperse through the rods and provides the energy for electron excitation in the conduction band [65]. The effectiveness of the TiO_2 Ag-FR film is also attributed to the intermediate Ti^{3+}-oxygen vacancy level that exists in the TiO_2. However, this only delays the recombination of the electron–hole pair by femtoseconds [66]. The probability of an electron and hole to recombine is high. Thus, the Ag metal will assist in charge separation by the formation of a Schottky barrier between TiO_2 and the Ag metal [31],[32]. This high barrier value inhibits the electron transfer back to the TiO_2. The Ag metal acts as a reservoir for the electron, suppresses the electron-hole recombination, and enhances the photodegradation of MB. Furthermore, the exposed facets of (1 1 0) and (1 1 1) also assist in enhancing photocatalytic activity by inducing spatial separation between the electron–hole pairs.

The decreased photogenerated charge carrier could be ascribed to the low degradation at high Ag content. The Ag dopant covers the active site of TiO_2 and limits the photonic permeation for photoexcitation of electron [35]. Conversely, the high Ag content causes the Ag metal to agglomerate, which increases the interface between the TiO_2 and Ag. The high-density defect, such as the surface state contained in the interface, could act as a recombination centre for electron and hole [64]. These issues lead to lower efficiency of the photocatalytic activity. The mechanism for photocatalytic degradation of MB is illustrated in Fig. 12. The proposed mechanism for the photocatalytic activity of the Ag-FR TiO_2 film towards MB degradation under UV light irradiation is described below [45]. The electron is excited from the valence band to the conduction band when irradiated with UV light (Eq. (7)). Next, the h^+ reacts with the hydroxyl group (OH^-) from the water or alkaline to form the hydroxyl radical that degrades the dye (Eqs. (8)–(9)).

$$TiO_2 + hv \rightarrow e^- + h^+ \quad (7)$$

$$h^+ + H_2O \rightarrow H^+ + OH^{\cdot} \quad (8)$$

$$h^+ + OH^- \rightarrow OH^{\cdot} \quad (9)$$

When the Ti^{4+} ions accept the electron while being exposed to UV irradiation on the TiO_2 catalyst, the formation of Ti^{3+} occurs. The

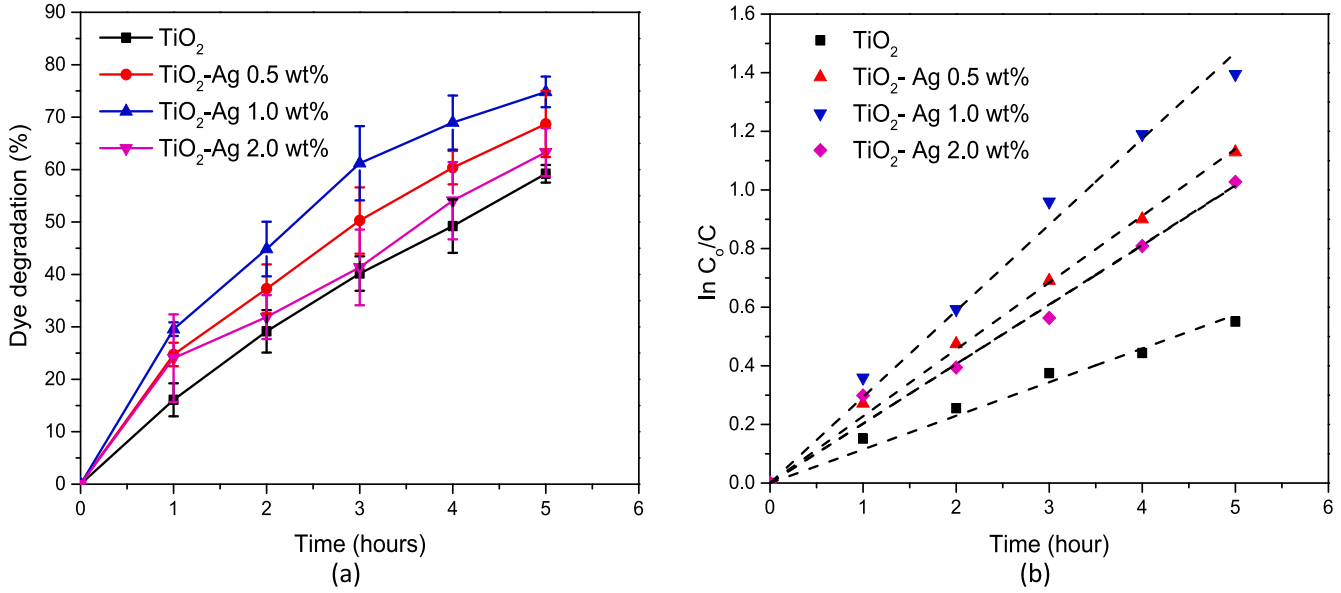

Fig. 11. (a) Photodegradation of MB [5 ppm of MB, pH 12]. The error bars correspond to the 95% confidence limit. (b) Kinetic Study for undoped TiO_2 and various amount of Ag dopant.

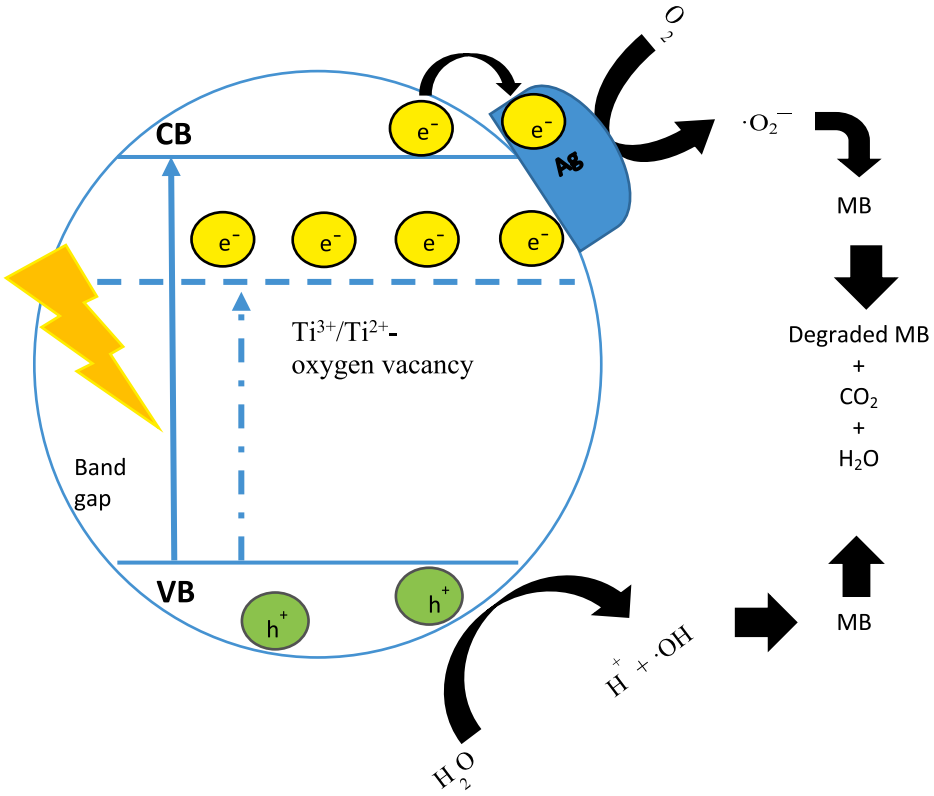

Fig. 12. The mechanism of photocatalytic activity for MB degradation.

electron is trapped and reduced Ti^{4+} to Ti^{3+} while the hole oxidises O_2^- anions to hole trapped (O^-) [61]. The electron is excited to the localised state and Ti^{4+} is reduced to lower oxidation states such as Ti^+, Ti^{2+}, and Ti^{3+} that act as an electron trap and suppresses the recombination between the electron–hole pairs [24], (Eqs. (10)–(13)).

$$e^- + Ti^{4+} \rightarrow Ti^{3+} \quad (10)$$

$$e^- + Ti^{3+} \rightarrow Ti^{2+} \quad (11)$$

$$Ti^{3+} + O_2 \rightarrow Ti^{4+} + {}^{\cdot}O_2^- \quad (12)$$

$$Ti^{2+} + O_2 \rightarrow Ti^{3+} + {}^{\cdot}O_2^- \quad (13)$$

From the XPS results, only Ag metal was detected. Ag becomes ionic upon irradiation (Eq. (14)). The electron flows to the Ag site and subsequently reduces the recombination between the electron and the hole (Eqs. (15)–(16)). Since the Fermi level of Ag is lower than TiO_2, it inhibits the electron from Ag from transferring back to TiO_2. This leads to the formation of the Schottky barrier at the interface between Ag—TiO_2 [63]. This phenomenon allows more reaction with O_2 to produce more reactive radical species (Eq. (17)).

$$Ag^0 + hv \rightarrow Ag^* \quad (14)$$

$$e^- + Ag^{+n} \rightarrow Ag^{n-1} \quad (15)$$

$$Ag^{n-1} + h^+ \rightarrow TiO_2 + Ag^{+n} \quad (16)$$

$$Ag^{n-1} + O_2 \rightarrow Ag^{+n} + {}^{\cdot}O_2^- \quad (17)$$

The trapped electron reacts with dissolved oxygen to form superoxide anions, while the hole reacts with water molecules or hydroxide ions to form hydroxyl radicals (Eqs. (18)–(19)). Both radicals attack the organic compound and degrade the dye [35], to produce degraded dyes with CO_2 and H_2O, which are not harmful to the environment (Eqs. (20)–(21)).

$$O_2^- + e^- + H^+ \rightarrow H_2O_2 \quad (18)$$

$$H_2O_2 \rightarrow OH^{\cdot} \quad (19)$$

$$O_2^- + \text{organic compound} \rightarrow CO_2 + H_2O \quad (20)$$

$$OH^{\cdot} + \text{organic compound} \rightarrow CO_2 + H_2O \quad (21)$$

Even though the degradation rate by the film is lower than that of powder catalyst, the film catalyst is more practical in reducing the cost of treatment. This is because it eliminates the need for post-separation between the catalyst and treated water. In contrast, the nanosized powder makes the post-separation more difficult with a higher probability of the catalyst passing through into the water stream, which can cause harm to aquatic lives.

4. Conclusion

Ag-FR TiO_2 films with various Ag content were successfully fabricated on FTO substrate using facile hydrothermal method. The Ag content was varied to obtain the optimum amount for the flowerlike rutile-phase TiO_2. The optimum Ag loading was 1.0 wt%. The surface morphologies of the Ag-FR TiO_2 film and the undoped TiO_2 with different exposed facets remain unchanged, which also enhanced the photocatalytic activity. When the amount of Ag content was increased, the intensity of the XRD peak decreased and FWHM value increased. The existing Ti^{3+}-oxygen vacancy defect is confirmed by the XPS and PL analyses. This defect creates shallow trap, suppresses recombination, and reduces band gap. However, it is insufficient to suppress the required time for recombination. The modification of TiO_2 using Ag dopant proves the ability of Ag to act as a reservoir for an electron to suppress the recombination caused by the Schottky barrier. The synergistic effect between the (1 1 0) and (1 1 1) facets and Ti^{3+}-oxygen vacancy from Ag play an important role in the reduction of TiO_2 band gap. It also acts as an electron trap for suppressing the recombination of electrons and holes to enhance the photocatalytic activity, thus extending the lifetime of the photogenerated electron and hole. The immobilised catalyst or film has great potential for wastewater treatment

aside from being a significant recent progress reported on film modification. In future, the authors propose to expand the investigation on the specific surface area, transient photocurrent, and the detection of reactive oxygen species to identify the major influences of Ag-FR TiO_2 film in photocatalytic degradation. The stability of the film is one of the important issues to be addressed before it can be applied in the industrial sector. The stable and smart responsive film with high endurance is a crucial factor for making cost-effective material to meet the industrial requirement. Hence, the potential reusability of the Ag-FR TiO_2 film needs to be examined in the future to determine its stability for industrial implementation.

Credit author statement

N.K.A. Hamed: Investigation, Writing - Original Draft. **M.K. Ahmad:** Conceptualization, Supervision. **N.H.H. Hairom:** Formal analysis, Validation. **A.B. Faridah:** Writing - Review & Editing, Resources. **A.B. Suriani:** Conceptualization, Methodology. **M.H. Mamat:** Writing - Review & Editing, Validation. **M. Shimomura:** Conceptualization, Supervision. **F.I.M. Fazli:** Conceptualization. **N. Nayan:** Writing - Editing. **S.M. Mokhtar:** Conceptualization, Methodology. **A. Mohamed:** Validation. **W.I.W. Omar:** Writing - Review.

Declaration of Competing Interest

The authors declare that they have no known competing financial interests or personal relationships that could have appeared to influence the work reported in this paper.

Acknowledgement

The authors acknowledge the financial support of the Research University Grant from Universiti Tun Hussein Onn (Tier 1 Vot U932 and GPPS Vot U958). The author would also like to thank the Center for Instrumental Analysis, Shizuoka University, Hamamatsu, Japan, Microelectronics, and Nanotechnology-Shamsuddin Research Centre (MiNT-SRC) for the characterisation equipment.

References

[1] A.L. Ahmad, S. Ismail, S. Bhatia, Water recycling from palm oil mill effluent (POME) using membrane technology, Desalination 157 (1–3) (2003) 87–95.
[2] A.O. Ibhadon, P. Fitzpatrick, Heterogeneous photocatalysis: recent advances and applications, Catalyst 3 (2013) 189.
[3] M. Haji, K. Sanaullah, S. Lim, S.A. Bhawani, T. Jamil, Photocatalytic treatment technology for palm oil mill effluent (POME) – a review, Process Saf. Environ. Prot. 102 (2016) 673.
[4] J.L.H. Chau, Y.M. Lin, A.K. Li, et al., Transparent high refractive index nanocomposite thin films, Mater. Lett. 61 (2007) 2908.
[5] O. Diwald, T.L. Thompson, T. Zubkov, E.G. Goralski, S.D. Walck, J.T. Yates, Photochemical activity of nitrogen-doped rutile TiO_2 (110) in visible light, J. Phys. Chem. B 2 (110) (2004) 6004.
[6] N.K.A. Hamed, Study on photocatalytic performance of rutile phased TiO2 microsize rods/flowers film towards methyl orange degradation, 2017.
[7] X.F. Lei, X.X. Xue, H. Yang, Preparation and characterization of Ag-doped TiO_2 nanomaterials and their photocatalytic reduction of Cr (VI) under visible light, Appl. Surf. Sci. 321 (2014) 396.
[8] J. Yu, W. Wang, B. Cheng, et al., Enhancement of photocatalytic activity of mesoporous TiO powders by hydrothermal surface fluorination treatment enhancement of photocatalytic activity of mesoporous TiO_2 powders by hydrothermal surface fluorination treatment, J. Phys. Chem. C 113 (6) (2009) 6743.
[9] K. Azad, P. Ganjanan, Photodegradation of methyl orange in aqueous solution by the visible light active Co:La: TiO_2 nanocomposite, Chem Sci J. 8 (03) (2017) 164.
[10] L.G. Devi, R. Kavitha, A review on plasmonic metal-TiO_2 composite for generation, trapping, storing and dynamic vectorial transfer of photogenerated electrons across the Schottky junction in a photocatalytic system, Appl. Surf. Sci. 360 (2016) 601–622.
[11] Z. Zhao, X. Zhang, G. Zhang, et al., Effect of defects on photocatalytic activity of rutile TiO_2 nanorods, Nano Res. 8 (12) (2015) 4061–4071.
[12] A. Alvaro, S. Ramirez, A.P. Prospero, M.C. Elay, Enhanced photocatalytic activity of TiO_2 film by modification with polyethylene glycol, Quim Nov. 35 (10) (2012) 1931–1935.
[13] J. Yan, G. Wu, L. Li, Understanding the effect of surface/bulk defects on the photocatalytic activity of TiO2: anatase versus rutile, Phys. Chem. 15 (5) (2013) 10978.
[14] H.S. Jung, H. Kim, Origin of low photocatalytic activity of rutile TiO_2, Electron. Mater. Lett. 5 (2) (2009) 73–76.
[15] X. Zhang, H. Cui, M. Humayun, et al., Exceptional performance of photoelectrochemical water oxidation of single-crystal rutile TiO_2 nanorods dependent on the hole trapping of modified chloride, Sci. Rep. 6 (2016) 1–8.
[16] M.M. Yusoff, M.H. Mamat, A.S. Ismail, et al., Low-temperature-dependent growth of titanium dioxide nanorod arrays in an improved aqueous chemical growth method for photoelectrochemical ultraviolet sensing, J. Mater. Sci.: Mater. Electron. 30 (2) (2019) 1017–1033.
[17] T. Huyen, T. Chi, N. Dung, H. Kosslick, N. Liem, Enhanced photocatalytic activity of {110}-faceted TiO_2 rutile nanorods in the photodegradation of hazardous pharmaceuticals, Nanomaterials 8 (5) (2018) 276.
[18] N. Masahashi, Y. Mizukoshi, S. Semboshi, N. Ohtsu, Enhanced photocatalytic activity of rutile TiO_2 prepared by anodic oxidation in a high concentration sulfuric acid electrolyte, Appl. Catal. B Environ. 90 (1–2) (2009) 255–261.
[19] Z. Pei, S. Weng, P. Liu, Enhanced photocatalytic activity by bulk trapping and spatial separation of charge carriers: a case study of defect and facet mediated TiO_2, Appl. Catal. B Environ. 180 (2016) 463–470.
[20] Y. Liu, S. Wang, P. Zheng, M. Ding, G. Yang, One-step synthesis of Ag-decorated Ti^{3+}-doped TiO_2 nanosheets with improved photocatalytic properties via deflagration method, Mater. Lett. 216 (2020) 127016.
[21] M. Khairy, W. Zakaria, Effect of metal-doping of TiO_2 nanoparticles on their photocatalytic activities toward the removal of organic dyes, Egypt J. Pet. 23 (4) (2014) 419.
[22] M. Miyauchi, A. Ikezawa, H. Tobimatsu, H. Irie, K. Hashimoto, Zeta potential and photocatalytic activity of nitrogen-doped TiO_2 thin films, PCCP 6 (4) (2004) 865.
[23] M. Li, H. Liu, T. Liu, Y. Qin, Design of a novel dual Z-scheme photocatalytic system composited of Ag_2O modified Ti^{3+} self doped TiO_2 nanocrystals with individual exposed (001) and (101) facets, Mater. Charact. 124 (2016) 136.
[24] S.A. Abdullah, M.Z. Sahdan, N. Nayan, Z. Embong, Neutron beam interaction with rutile TiO_2 single crystal Raman and XPS study on Ti^{3+} – oxygen vacancy formation, Mater. Lett. 111 (2019) 127143.
[25] X. Zhou, V. Haublein, N. Liu, et al., TiO_2 nanotubes: nitrogen-ion implantation at low dose provides noble-metal-free photocatalytic H_2-evolution activity, Angew Chemie-Int. Ed. 55 (11) (2016) 3763.
[26] S. Pan, X. Liu, M. Guo, et al., Engineering the intermediate band states in amorphous Ti^{3+}-doped TiO_2 for hybrid dye-sensitized solar cell applications, J. Mater. Chem. A 3 (21) (2015) 11437.
[27] S.K. Md Saad, A. Ali Umar, M.I. Ali Umar, et al., Two-dimensional, hierarchical Ag-doped TiO2 nanocatalysts: effect of the metal oxidation state on the photocatalytic, ACS Omega 3 (3) (2018) 2579–2587.
[28] W. Kallel, S. Chaabene, S. Bouattour, Novel (Ag, Y) doped TiO_2 plasmonic photocatalyst with enhanced photocatalytic activity under visible light, Physicochem. Probl. Miner Process. 55 (3) (2019) 745–759.
[29] X. Wang, X. Hou, W. Luan, D. Li, K. Yao, The antibacterial and hydrophilic properties of silver-doped TiO_2 thin films using sol-gel method silver, Appl. Surf. Sci. 258 (20) (2012) 8241.
[30] T. Ali, A. Ahmed, U. Alam, I. Uddin, P. Tripathi, M. Muneer, Enhanced photocatalytic and antibacterial activities of Ag-doped TiO2 nanoparticles under visible light, Mater. Chem. Phys. 212 (2018) 325.
[31] C. Peng, W. Wang, W. Zhang, Y. Liang, L. Zhuo, Surface plasmon-driven photoelectrochemical water splitting of TiO_2 nanowires decorated with Ag nanoparticles under visible light illumination, Appl. Surf. Sci. 420 (2017) 286–295.
[32] M.K. Kumar, K. Bhavani, G. Naresh, B. Srinivas, A. Venugopal, Plasmonic resonance nature of Ag-Cu/TiO_2 photocatalyst under solar and artificial light: synthesis, characterization and evaluation of H_2O splitting activity, Appl. Catal. B Environ. 199 (2016) 282–291.
[33] Y.X. Dong, X.L. Wang, E.M. Jin, S.M. Jeong, B. Jin, S.H. Lee, One-step hydrothermal synthesis of Ag decorated TiO2 nanoparticles for a dye-sensitized solar cell application, Renew. Energy 135 (2019) 1207.
[34] G. Zhou, H. Meng, Y. Cao, et al., Surface plasmon resonance-enhanced solar-driven photocatalytic performance from Ag nanoparticles-decorated Ti^{3+} self-doped porous black TiO_2 pillars, J. Ind. Eng. Chem. 64 (2018) 188–193.
[35] S. Demirci, T. Dikici, M. Yurddaskal, S. Gultekin, Synthesis and characterization of Ag-doped TiO_2 heterojunction films and their photocatalytic performances, Appl. Surf. Sci. 390 (2016) 591.
[36] S. Perumal, K. Monikandaprabu, C.G. Sambandam, A.P. Mohamed, Synthesis and characterization studies of solvothermally synthesized undoped and Ag-doped TiO_2 nanoparticles using toluene as a solvent, Int. J. Eng. Res. Appl. 4 (7) (2014) 184.
[37] P. Chen, A novel synthesis of Ti^{3+} self-doped Ag_2O/TiO_2 (p-n) nanoheterojunctions for enhanced visible photocatalytic activity, Mater. Lett. 163 (2016) 130.
[38] M.K. Ahmad, A. Fitrah, A. Aziz, C.F. Soon, N. Nafarizal, Rutile Phased Titanium Dioxide (TiO2) Nanorod/Nanoflower Based Waste Water Treatment Device, 2017.
[39] M.M. Mohamed, M.S. Al-Sharif, Visible light assisted reduction of 4-nitrophenol to 4-aminophenol on Ag/TiO_2 photocatalysts synthesized by hybrid templates, Appl. Catal. B Environ. 142–143 (2013) 432.
[40] F. Bensouici, T. Souier, A.A. Dakhel, A. Iratni, M. Bououdina, Synthesis, characterization and photocatalytic behaviour of Ag-doped TiO_2 thin film, Superlatt. Microstruct. 85 (2015) 255.
[41] M.M. Yusoff, M.M. Mamat, A.S. Ismail, et al., Enhancing the performance of self-powered ultraviolet photosensor using rapid aqueous chemical-grown Aluminium-doped titanium oxide nanorod arrays as an electron transport layer, Thin Solid Films 655 (2018) 1.
[42] N.K.A. Hamed, Influence of hydrochloric acid volume on the growth of titanium

dioxide (TiO_2) nanostructures by hydrothermal method, Sains Malaysiana. 45 (11) (2016) 1669.
[43] M.K. Ahmad, S.M. Mokhtar, C.F. Soon, et al., Raman investigation of rutile-phased TiO_2 nanorods/nanoflowers with various reaction times using a one-step hydrothermal method, J. Mater. Sci.: Mater. Electron. 27 (8) (2016) 7920.
[44] J.V. Hernández, S. Coste, A.G. Murillo, F.C. Romo, A. Kassiba, Effects of metal doping (Cu, Ag, Eu) on the electronic and optical behaviour of nanostructured TiO_2, J. Alloys Compd. 710 (2017) 355.
[45] L.M. Santos, W.A. Machado, M.D. Franca, et al., Structural characterization of Ag-doped TiO_2 with enhanced photocatalytic activity, RSC Adv. 5 (125) (2015) 103752.
[46] Z. Lai, F. Peng, et al., A new insight into regulating high energy facets of rutile TiO_2, J. Mater. Chem. A 111 (2013) 1–4.
[47] T. Dhandayuthapani, R. Sivakumar, R. Ilangovan, Growth of micro flower rutile TiO_2 films by chemical bath deposition technique: study on the properties of structural, surface morphological, vibrational, optical and compositional, Surf. Interfaces 4 (2016) 59.
[48] V. Jordan, U. Javornik, J. Plavec, A. Podgornik, A. Recnik, Self-assembly of multilevel branched rutile-type TiO_2 structures via oriented lateral and twin attachment, Sci. Rep. 6 (4) (2016) 1–13.
[49] A.A. Jalil, M. Mohamed, S. Triwahyono, N.S. Hassan, New insight into self-modified surfaces with defect-rich rutile TiO2 as a visible-light-driven photocatalyst, J Clean Prod. 168 (10) (2017) 1150–1162.
[50] R.V. Nair, M. Jijith, V.S. Gummaluri, C. Vijayan, A novel and efficient surfactant-free synthesis of Rutile TiO_2 microflowers with enhanced photocatalytic activity, Opt. Mater. (Amst.) 55 (2016) 38.
[51] N. Kamalia, Influence of hydrochloric acid volume on the growth of titanium dioxide (TiO_2) nanostructures by hydrothermal method, Sains Malaysiana 45 (11) (2016) 1669–1673.
[52] M. Ye, H.Y. Liu, C. Lin, Z. Lin, Hierarchical rutile TiO_2 flower cluster-based high efficiency dye-sensitized solar cells via direct hydrothermal growth on conducting substrates, Small 9 (2) (2013) 312.
[53] J. Su, J. Chen, Self-modification of titanium dioxide materials by Ti^{3+} and/or oxygen vacancies: new insights into defect chemistry of metal oxides, RSC Adv. 4 (2014) 13979–13988.
[54] P.M. Oliver, G.W. Watson, E.T. Kelsey, S.C. Parker, Atomistic simulation of the surface structure of TiO2 polymorphs rutile and anatase, J. Mater. Chem. 7 (3) (1997) 563–568.
[55] R. Lopez, R. Gomez, Band-gap energy estimation from diffuse reflectance measurements on sol-gel and commercial TiO_2: a comparative study, J. Sol-Gel Sci. Technol. 61 (1) (2012) 1.
[56] A.M. Selman, Z. Hassan, M. Husham, Structural and photoluminescence studies of rutile TiO_2 nanorods prepared by chemical bath deposition method on Si substrates at different pH values, Meas. J. Int. Meas. Confed. 56 (2014) 155.
[57] S. Mathew, A.K. Prasad, T. Benoy, P.P. Rakesh, M. Hari, T.M. Libish, P. Radhakrishnan, V.P.N. Nampoori, C.P.G. Vallabhan, UV-visible photoluminescence of TiO_2 nanoparticles prepared by hydrothermal method, J. Fluoresc. 22 (6) (1563.) 2012.
[58] X. Pan, M. Yang, N. Zhang, Defective TiO_2 with oxygen vacancies: Synthesis, properties and photocatalytic applications, Nanoscale 5 (2013) 3601.
[59] L. Xiong, J. Li, B. Yang, Y. Yu, Ti^{3+} in the surface of titanium dioxide: generation, properties and photocatalytic application, J. Nanomater. 2012 (2011) 1.
[60] L. Le, J. Xu, Z. Zhou, H. Wang, R. Xiong, J. Shi, Effect of oxygen vacancies and Ag deposition on the magnetic properties of Ag/N co-doped TiO_2 single-crystal films, Mater. Res. Bull. 102 (2018) 337.
[61] L.B. Xiong, J.L. Li, B. Yang, Y. Yu, Ti^{3+} in the surface of titanium dioxide: generation, properties and photocatalytic application, J Nanomater 2012 (2011) 1.
[62] M. Ahamed, M.A.M. Khan, M.J. Akhtar, H.A. Alhadlaq, Ag-doping regulates the cytotoxicity of TiO_2 nanoparticles via oxidative stress in human cancer cells, Sci. Rep. 11 (2017) 1.
[63] Y. Zhang, T. Wang, M. Zhou, Y. Wang, Z. Zhang, Hydrothermal preparation of Ag-TiO2 nanostructures with exposed 001}/{101 facets for enhancing visible light photocatalytic activity, Ceram. Int. 43 (3) (2017) 3118.
[64] F. Bensouici, T. Souier, A.A. Dakhel, A. Iratni, R. Tala-ighil, M. Bououdina, Synthesis, characterization and photocatalytic behaviour of Ag-doped TiO_2 thin film, Superlattices Microstruct. 85 (2015) 255.
[65] H. Li, X. Shen, Y. Liu, L. Wang, J. Lei, J. Zhang, Facile phase control for hydrothermal synthesis of anatase-rutile TiO_2 with enhanced photocatalytic activity, J. Alloys Compd. 646 (2015) 380.
[66] J. Schneider, M. Matsuoka, M. Takeuchi, et al., Understanding TiO_2 photocatalysis: mechanisms and materials, Am. Chem. Soc. 114 (2014) 9919.